

# Breaking Badly: DFT-D2 Gives Sizeable Errors for Tensile Strengths in Palladium-Hydride Solids

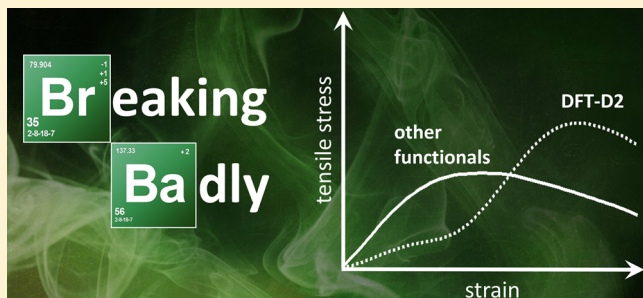
Niranjan V. Ilawe,<sup>†</sup> Jonathan A. Zimmerman,<sup>‡</sup> and Bryan M. Wong<sup>\*,†</sup>

<sup>†</sup>Department of Chemical & Environmental Engineering and Materials Science & Engineering Program, University of California-Riverside, Riverside, California 92521, United States

<sup>‡</sup>Hydrogen and Combustion Technologies Department, Sandia National Laboratories, Livermore, California 94551, United States

## S Supporting Information

**ABSTRACT:** Dispersion interactions play a crucial role in noncovalently bound molecular systems, and recent studies have shown that dispersion effects are also critical for accurately describing covalently bound solids. While most studies on bulk solids have solely focused on equilibrium properties (lattice constants, bulk moduli, and cohesive energies), there has been little work on assessing the importance of dispersion effects for solid-state properties far from equilibrium. In this work, we present a detailed analysis of both equilibrium and highly nonequilibrium properties (tensile strengths leading to fracture) of various palladium-hydride systems using representative DFT methods within the LDA, GGA, DFT-D2, DFT-D3, and nonlocal vdW-DFT families. Among the various DFT methods, we surprisingly find that the empirically constructed DFT-D2 functional gives extremely anomalous and qualitatively incorrect results for tensile strengths in palladium-hydride bulk solids. We present a detailed analysis of these effects and discuss the ramifications of using these methods for predicting solid-state properties far from equilibrium. Most importantly, we suggest caution in using DFT-D2 (or other coarse-grained parametrizations obtained from DFT-D2) for computing material properties under large stress/strain loads or for evaluating solid-state properties under extreme structural conditions.



## INTRODUCTION

Ductile metals and their alloys play a crucial role in structural materials due to their widespread use in large-scale construction and architectural applications. Because of their intrinsic ability to smoothly deform under tensile stress, these materials are extensively used in electrical wires, semiflexible inorganic membranes, and structural materials for long-term storage.<sup>1–4</sup> Since the structural properties of these materials are highly dependent on their atomic composition, there has been increased interest in using first-principles calculations to predict their mechanical properties to provide guidance for industrial manufacturing initiatives.<sup>5–10</sup> Most notably, the use of first-principles calculations is crucial to the development of new, physically based constitutive models for continuum-scale modeling and mesoscale systems.<sup>11–19</sup> In this context, over the past several years our group has focused on the development and use of both density functional theory (DFT) and molecular dynamics (MD) methods for characterizing complex palladium-based materials and their alloys.<sup>20,21</sup> Our motivation stems from the widespread use of palladium in enabling technological advancements for both structural and hydrogen-storage applications. By far, the largest usage of palladium resides in catalytic converters for the auto industry and their use as catalytic materials in the agrochemical, pharmaceutical, and materials-based sectors.<sup>22,23</sup> Within the

hydrogen-storage and production industries, palladium is widely used in membrane reactors for the production of high-purity hydrogen,<sup>24</sup> and palladium-based alloys are actively used in new fuel cell technologies as replacements for costly platinum-based alloys.<sup>25</sup>

At room temperature, pure palladium reacts with both molecular and atomic hydrogen to form various palladium-hydride ( $\text{PdH}_x$ ) stoichiometries.<sup>26</sup> As depicted in Figure 1, these metal-hydride materials are formed when hydrogen atoms become embedded into various interstitial sites within the metal lattice.<sup>20,21</sup> Since the hydrogen absorption process in palladium is reversible,<sup>27</sup> there is significant interest in using palladium-based alloys for large-scale storage of hydrogen and their isotopes. While there has been considerable work in examining the equilibrium hydrogen-storage properties of palladium, practical applications of these materials are still limited by their intrinsic dynamical embrittlement caused by the growth of gaseous bubbles in the lattice. In particular, several experimental and computational studies have shown that palladium-hydride materials containing large amounts of hydrogen are more susceptible to brittle fracture than their pure metallic counterparts.<sup>28</sup> In order to fully characterize these

Received: July 8, 2015

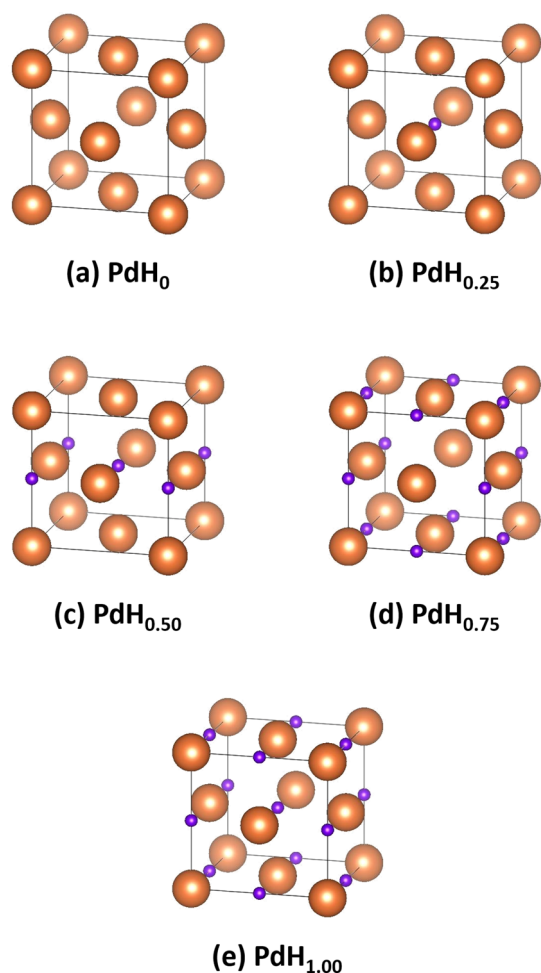


**Figure 1.** Unit cells for various PdH<sub>x</sub> stoichiometries where  $x =$  (a) 0, (b) 0.25, (c) 0.50, (d) 0.75, and (e) 1.00. The large orange spheres represent Pd atoms, and the small purple spheres denote the placement of H atoms.

complex materials, it is necessary to carry out detailed predictions of *both* their equilibrium and nonequilibrium structural properties to understand the limitations of first-principle-based methods for these processes. While it is obvious that dispersion-corrected DFT methods play a significant role in materials characterized by noncovalent interactions (i.e., graphene-based systems,<sup>29,30</sup> nanotube aggregates,<sup>31</sup> and layered materials<sup>32</sup>), prior studies have shown that dispersion interactions still play a dominant role in *covalently bonded* bulk solids.<sup>33</sup> In particular, we focus on the implications of using various dispersion-corrected DFT methods for predicting the mechanical properties of various PdH<sub>x</sub> materials to serve as guidance for experiment and also as critical benchmarks for constructing new Pd–H MD force fields.

Although most work on dispersion-corrected methods has focused on predicting properties of molecular systems at equilibrium (i.e., structures and energies at a global minimum), there has been significantly less work on understanding the performance of these methods for systems far from equilibrium. In particular, there is mounting evidence in the scientific literature demonstrating the importance of including nonequilibrium geometries and energies to construct new dispersion-corrected DFT methods that are globally accurate.<sup>34,35</sup> While there has been increased effort to incorporate

these effects in molecular systems, we are not aware of any prior studies using dispersion-based DFT methods for *bulk solids far from equilibrium* (i.e., strained up to their maximum tensile strength). To bridge this knowledge gap, we carry out an extensive series of DFT calculations on both equilibrium (optimized geometries, bulk moduli, and cohesive energies) as well as nonequilibrium properties (stress–strain relationships and maximum tensile strength) in various PdH<sub>x</sub> systems. We demonstrate that dispersion effects play a vital role in these complex solids, and, most importantly, we show that some dispersion-corrected functionals can give spurious, *qualitatively incorrect* results for structural properties of solids far from equilibrium. We give a detailed analysis of both the equilibrium and nonequilibrium properties predicted by the various DFT methods, and we discuss the implications of using these methods in developing new DFT parametrizations and fitted MD force fields for these materials.

## THEORY AND METHODOLOGY

Since the main purpose of this work is to assess the consequences of using dispersion-corrected DFT methods for both equilibrium and nonequilibrium processes in bulk solids, we briefly summarize the underlying theories for these methods. In addition to benchmarking common DFT methods within the LDA and GGA family of functionals, we investigated several different classes of dispersion-corrected methods: three empirically constructed approaches: DFT-D2,<sup>36</sup> DFT-D3,<sup>37</sup> and DFT-TS<sup>38,39</sup> and the fully nonlocal vdW-based methods.<sup>33,40,41</sup> Within the DFT-D2 approach, an empirical atomic pairwise dispersion correction is added to the Kohn–Sham portion of the total energy ( $E_{\text{KS-DFT}}$ ) as

$$E_{\text{DFT-D}} = E_{\text{KS-DFT}} + E_{\text{disp}} \quad (1)$$

where  $E_{\text{disp}}$  is given by

$$E_{\text{disp}} = - \sum_{i=1}^{N_{\text{at}}-1} \sum_{j=i+1}^{N_{\text{at}}} \sum_{\mathbf{g}} f_{\text{d},6}(R_{ij,\mathbf{g}}) \frac{C_{6,ij}}{R_{ij,\mathbf{g}}^6} \quad (2)$$

The summation is over all atom pairs  $i$  and  $j$  and over all  $\mathbf{g}$  lattice vectors with the exclusion of the  $i = j$  contribution when  $\mathbf{g} = 0$  (this restriction prevents atomic self-interaction in the reference cell). The parameter  $C_{6,ij}$  is the dispersion coefficient for atom pairs  $i$  and  $j$ , calculated as the geometric mean of the atomic dispersion coefficients.  $R_{ij,\mathbf{g}}$  is the interatomic distance between atom  $i$  in the reference cell and  $j$  in the neighboring cell at distance  $|\mathbf{g}|$ . In order to avoid near-singularities for small interatomic distances,  $f_{\text{d},6}$  is a damping function that effectively rescales interatomic forces to minimize interactions within the bonding distance  $R_{ij,\mathbf{g}}$ .

A significant improvement over the DFT-D2 method is the DFT-D3 scheme, which is characterized by higher accuracy, a broader range of applicability, and less empiricism compared to the DFT-D2 method. The D3 correction scheme by Grimme et al.<sup>37</sup> uses the following form of the dispersion correction

$$E_{\text{disp}} = - \sum_{i=1}^{N_{\text{at}}-1} \sum_{j=i+1}^{N_{\text{at}}} \sum_{\mathbf{g}} f_{\text{d},6}(R_{ij,\mathbf{g}}) \frac{C_{6,ij}}{R_{ij,\mathbf{g}}^6} + f_{\text{d},8}(R_{ij,\mathbf{g}}) \frac{C_{8,ij}}{R_{ij,\mathbf{g}}^8} \quad (3)$$

where  $f_{\text{d},8}$  and  $C_{8,ij}$  are eighth-order damping functions and dispersion coefficients, respectively, for the additional  $R_{ij,\mathbf{g}}^{-8}$  repulsive potential. However, unlike the DFT-D2 method, the  $C_{6,ij}$  dispersion coefficients are geometry dependent and are

adjusted as a function of the local geometry around atoms  $i$  and  $j$ . In the original DFT-D3 method, the  $f_{d,6}$  and  $f_{d,8}$  damping functions (and thus  $E_{\text{disp}}$ ) were constructed to approach zero when  $R_{ij} = 0$ . A critical disadvantage of this zero-damping approach is that at small and medium distances, the atoms experience repulsive forces leading to even longer interatomic distances than those obtained without dispersion corrections.<sup>42</sup> As a practical solution for this counterintuitive observation, Becke and Johnson<sup>43–45</sup> proposed the DFT-D3(BJ) method which contains modified expressions for  $f_{d,6}$  and  $f_{d,8}$  that lead to a constant contribution of  $E_{\text{disp}}$  to the total energy when  $R_{ij} = 0$ . The DFT-D3(BJ) method produces improved results for nonbonded distances/energies,<sup>42</sup> and we use this variant of the D3 damping function throughout this work.

Within the same family of empirically constructed dispersion methods is the DFT-TS method proposed by Tkatchenko and Scheffler,<sup>38,39</sup> which has also been previously applied to molecular solids.<sup>46</sup> While the expression for the dispersion correction in DFT-TS is identical to the DFT-D2 method (eq 2), the important distinction is that the dispersion coefficients and damping function in DFT-TS are explicitly dependent on the charge-density. As such, the DFT-TS method takes into account van der Waals interactions due to the local chemical environment by directly calculating the polarizability, dispersion coefficients, and atomic radii from their free-atomic values.<sup>38</sup>

Finally, beyond the semiempirical additive approaches used in the previous methods, there has been significant effort during the past decade in constructing new functionals that explicitly calculate van der Waals (vdW) correlation effects. Specifically, the vdW-DF methods proposed by Dion et al.<sup>41</sup> incorporate these dispersion forces by evaluating *nonlocal* double real-space integrals of the electron density to include these correlation effects. In addition to the original vdW-DF approach,<sup>41</sup> there have been several additional improvements including a revised vdW-DF2 kernel<sup>47</sup> as well as the “opt” family of functionals<sup>33</sup> (optPBE-vdW, optB88-vdW, and optB86b-vdW). In all of these nonlocal vdW functionals, the exchange-correlation energy,  $E_{\text{xc}}$ , takes the form

$$E_{\text{xc}} = E_{\text{x}}^{\text{GGA}} + E_{\text{c}}^{\text{LDA}} + E_{\text{c}}^{\text{nl}} \quad (4)$$

where  $E_{\text{x}}^{\text{GGA}}$  is the GGA exchange energy,  $E_{\text{c}}^{\text{LDA}}$  accounts for the local correlation energy within the local density approximation, and  $E_{\text{c}}^{\text{nl}}$  is the nonlocal correlation energy. An important distinguishing characteristic of these nonlocal vdW functionals (compared to the DFT-D approaches) is that they directly incorporate van der Waals effects explicitly in the exchange-correlation kernel as a nonlocal double real space integral of the electron density without assuming *a priori* an analytic form for the dispersion interaction.

For all of the calculations in this work, we used a locally modified version of the VASP code for calculating the ideal tensile strength along different crystallographic directions (described further in the section on stress-strain properties). A planewave energy cutoff of 500 eV was used in conjunction with a dense  $15 \times 15 \times 15$  Monkhorst–Pack grid for sampling the Brillouin zone. All calculations utilized projected augmented wave (PAW) pseudopotentials, and a Gaussian smearing scheme with a 0.2 eV width was used to describe the partial occupancies for all the Pd-based solids.

## RESULTS AND DISCUSSION

**Lattice Constants, Bulk Moduli, and Cohesive Energies.** Before proceeding to an analysis of nonequilibrium stress-strain properties in the various  $\text{PdH}_x$  systems, it is necessary to first characterize the static properties of these solids. While the static properties of pure Pd are well-known, the lattice constants, bulk moduli, and cohesive energies of the other palladium-hydride systems are not well characterized. To serve as benchmarks for our survey of various DFT methods, we calculated the lattice constants and bulk moduli of pure Pd and compared their predicted values against experiment.<sup>48</sup> The predicted lattice constant and bulk moduli for Pd are presented in Table 1, and the relative errors between the predicted and experimental values are summarized in Figure 2(a).

**Table 1. Lattice Constants and Bulk Moduli for Pure Pd As Predicted by Various DFT Methods<sup>a</sup>**

	lattice constant (Å)		bulk modulus (GPa)	
	pure Pd	error	pure Pd	error
LDA	3.839	−0.92%	223	14.6%
PBE	3.946	1.84%	167	−14.4%
PBE-D2	3.890	0.39%	164	−16.1%
PBE-D3(BJ)	3.890	0.39%	188	−3.4%
PBE-TS	3.917	1.07%	183	−6.4%
vdW-DF2	4.095	5.68%	119	−38.9%
optB86b-vdW	3.903	0.73%	183	−6.3%

<sup>a</sup>The experimental lattice constant and bulk modulus for Pd is 3.875 Å and 195 GPa, respectively.<sup>48</sup>

As shown in Figure 2(a), LDA slightly underestimates the lattice constant for pure Pd. This error is not surprising, as bond lengths in LDA are typically underestimated due to the simplistic homogeneous electron gas approximation within the LDA exchange-correlation potential. The second-generation vdW-DF2 functional by Langreth and co-workers significantly overestimates the lattice constant compared to all of the tested methods. This error in the vdW-DF2 functional is consistent with the previous study by Klimeš et al.<sup>33</sup> which found that vdW-DF2 has average relative errors of 2.6% in the lattice constants for various solids. The semilocal PBE functional also overestimates the lattice constant, although the error is surprisingly not as severe as the vdW-DF2 predictions. The PBE-D2, PBE-D3(BJ), PBE-TS, and the nonlocal optB86b-vdW functionals give the best agreement to experiment, with the PBE-D2 and PBE-D3(BJ) functionals only performing marginally better than PBE-TS and optB86b-vdW.

Figure 2(b) compares the predicted bulk moduli for the various DFT methods against experiment. As expected, the bulk moduli follow the opposite trends as the lattice constant – DFT methods with small lattice constants typically exhibit large bulk moduli and vice versa. Most notably, LDA overestimates the bulk modulus for pure Pd, whereas vdW-DF2 significantly underestimates the bulk modulus by −38.9%. In contrast to the previous trends in the lattice constant, PBE-D2 does not perform as well and underestimates the bulk modulus by −16.1%, similar to the uncorrected PBE functional. The PBE-D3(BJ), PBE-TS, and optB86b-vdW methods all give the best agreement to experiment, with the PBE-D3(BJ) functional again only performing slightly better than PBE-TS and optB86b-vdW.



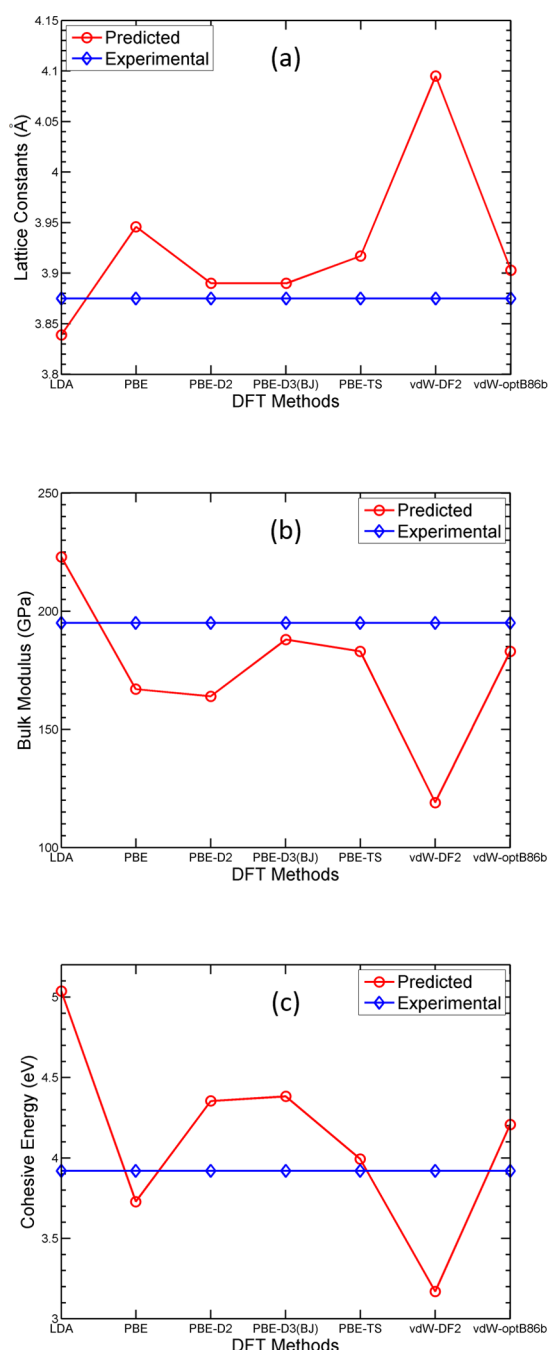


**Figure 2.** (a) Lattice constants, (b) bulk moduli, and (b) cohesive energies of pure palladium predicted by various DFT methods.

To complement the lattice constant and bulk moduli calculations described previously, we also calculated the cohesive energies (defined as the energy required for separating the condensed material into isolated free atoms) of all the various  $\text{PdH}_x$  systems using the expression

$$E_{\text{cohesive}} = n_{\text{Pd}}E_{\text{Pd}} + n_{\text{H}}E_{\text{H}} - E_{\text{PdH}_x} \quad (5)$$

where  $n_{\text{Pd}}$  is the number of palladium atoms in the  $\text{PdH}_x$  system,  $E_{\text{Pd}}$  is the energy of an isolated palladium atom,  $n_{\text{H}}$  is the number of hydrogen atoms in the  $\text{PdH}_x$  system,  $E_{\text{H}}$  is the energy of an isolated hydrogen atom, and  $E_{\text{PdH}_x}$  is the total electronic energy of the total  $\text{PdH}_x$  system. Based on its definition, the cohesive energy provides an indirect measure of

the stability of the material (with larger positive values indicating more stability) relative to the atomic elements. The calculated cohesive energies are presented in Table 2, and

**Table 2.** Cohesive Energies for Various  $\text{PdH}_x$  Stoichiometries, As Predicted by Various DFT Methods<sup>a</sup>

	$\text{PdH}_0$	$\text{PdH}_{0.25}$	$\text{PdH}_{0.50}$	$\text{PdH}_{0.75}$	$\text{PdH}_{1.00}$
LDA	5.036	4.606	4.328	4.130	3.974
PBE	3.728	3.459	3.284	3.156	3.051
PBE-D2	4.354	3.969	3.721	3.544	3.403
PBE-D3(BJ)	4.383	4.001	3.754	3.575	3.432
PBE-TS	3.993	3.689	3.491	3.349	3.233
vdW-DF2	3.169	2.976	2.849	2.754	2.674
optB86b-vdW	4.208	3.879	3.668	3.516	3.394

<sup>a</sup>The experimental cohesive energy for pure  $\text{PdH}_0$  is 3.92 eV.<sup>48</sup>

the relative difference between the predicted and experimental values for pure Pd is summarized in Figure 2(c). The experimental cohesive energy for pure Pd, corrected for zero-point energy effects, is 3.92 eV as obtained from ref 48.

Figure 2(c) provides a complementary viewpoint of chemical bonding in comparison to the lattice constants plotted in Figure 2(a). As expected, Figure 2(c) shows an opposite trend in the lattice constant compared to Figure 2(a) – DFT methods that predict a smaller lattice constant also yield a higher cohesive energy (i.e., stronger bonding) and vice versa. As such, the trends in the cohesive energy can be rationalized using the same arguments previously discussed for the lattice constant. For example, Figure 2(b) shows that LDA significantly overestimates the cohesive energy for Pd, which is consistent with the small lattice constant predicted by LDA in Figure 2(a). Interestingly, the vdW-DF2 functional underestimates the cohesive energy with a similar magnitude as the overestimation by LDA. This error in the vdW-DF2 functional is also consistent with the previous analyses by Klimeš et al.<sup>33</sup> which found that vdW-DF2 has quite large relative errors of  $-15.9\%$  in the atomization energies for various solids. These large errors have been observed in many other systems<sup>33,49,50</sup> and can be attributed to the steep behavior of the vdW-DF2 functional which at short distances is still too repulsive.<sup>51</sup> Both the PBE-D2 and PBE-D3(BJ) functionals overestimate the cohesive energy, although the error is not as severe as the LDA predictions. The PBE, PBE-TS, and the nonlocal vdW-optB86b functionals give the best agreement to experiment, with PBE slightly underestimating the cohesive energy compared to PBE-TS and vdW-optB86b.

Finally, Figure 3 summarizes the cohesive energy trends of the remaining  $\text{PdH}_x$  systems ( $x = 0, 0.25, 0.50, 0.75$ , and  $1.00$ ; cf. Figure 1) for all the various DFT methods. Again, we have chosen these specific stoichiometries based on our previous molecular dynamics study of thermodynamically stable  $\text{PdH}_x$  configurations for these materials.<sup>20,21</sup> While there are distinct differences between the magnitudes of the cohesive energies, it is important to mention that all DFT methods predict the cohesive energy in the  $\text{PdH}_x$  systems to decrease as the percentage of H in the metal-hydride lattice increases. These observations, coupled with our previous discussion of cohesive energies, corroborate the effects of embrittlement due to the presence of hydrogen in these materials.

**Stress–Strain Relationships.** With the static equilibrium properties now fully characterized for each of the DFT methods, we turn our attention to nonequilibrium stress–

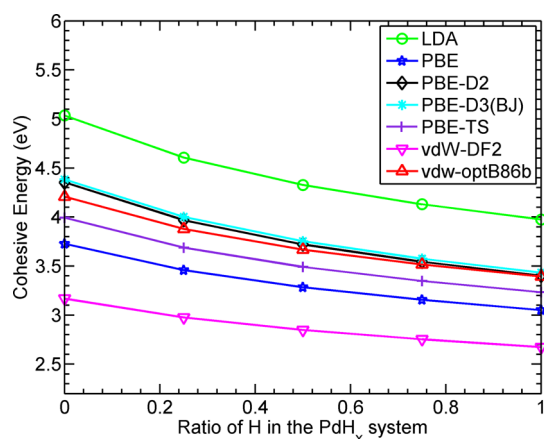


**Figure 3.** Cohesive energy trends as a function of hydrogen percentage in the  $\text{PdH}_x$  system as predicted by the various DFT methods.

strain effects. For uniaxial tensile strain, we calculated the tensile stress using the expression

$$\sigma = \frac{1}{V(\varepsilon)} \frac{\partial E}{\partial \varepsilon} \quad (6)$$

where  $\varepsilon$  is the imposed tensile strain,  $E$  is the total electronic energy, and  $V(\varepsilon)$  is the volume at the imposed tensile strain  $\varepsilon$ . The stress–strain curves are generated by first starting with the fully relaxed geometry and subsequently applying a fixed tensile strain ( $\varepsilon$ ) by elongating the crystal along a specified loading axis (described further below). The VASP source code was modified to perform constrained relaxations in the directions perpendicular to the elongation axis to minimize the other 5 independent components of the stress tensor and to ensure uniaxial loading. This important modification allows us to (1) account for the Poisson ratio of the material by relaxing the lattice constants in the directions perpendicular to the applied stress and (2) simultaneously allow for relaxation of the atomic positions in the material. In order to obtain smooth plots of the

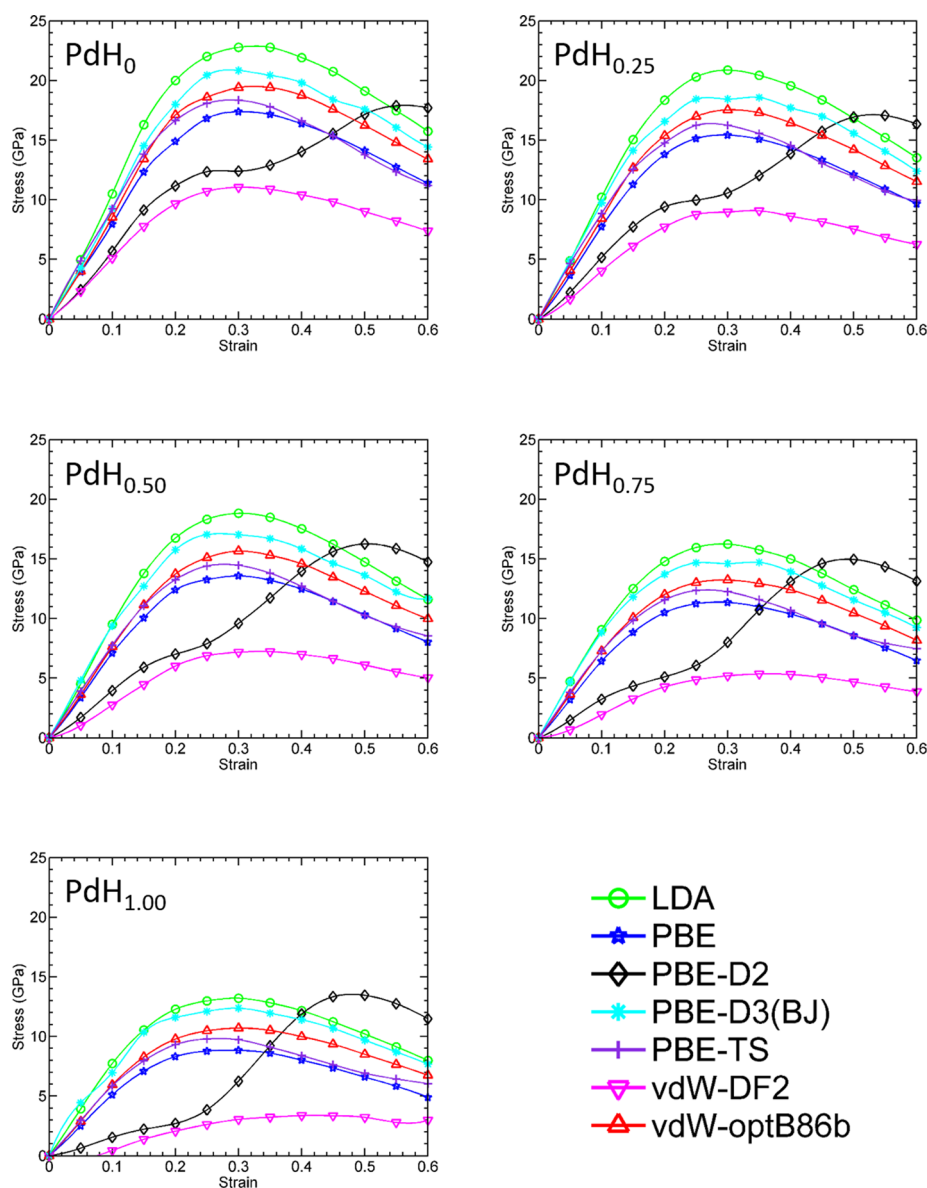


**Figure 4.** Stress–strain curves in  $\text{PdH}_x$  for  $x =$  (a) 0, (b) 0.25, (c) 0.50, (d) 0.75, and (e) 1.00 along the  $[100]$  crystal axis.

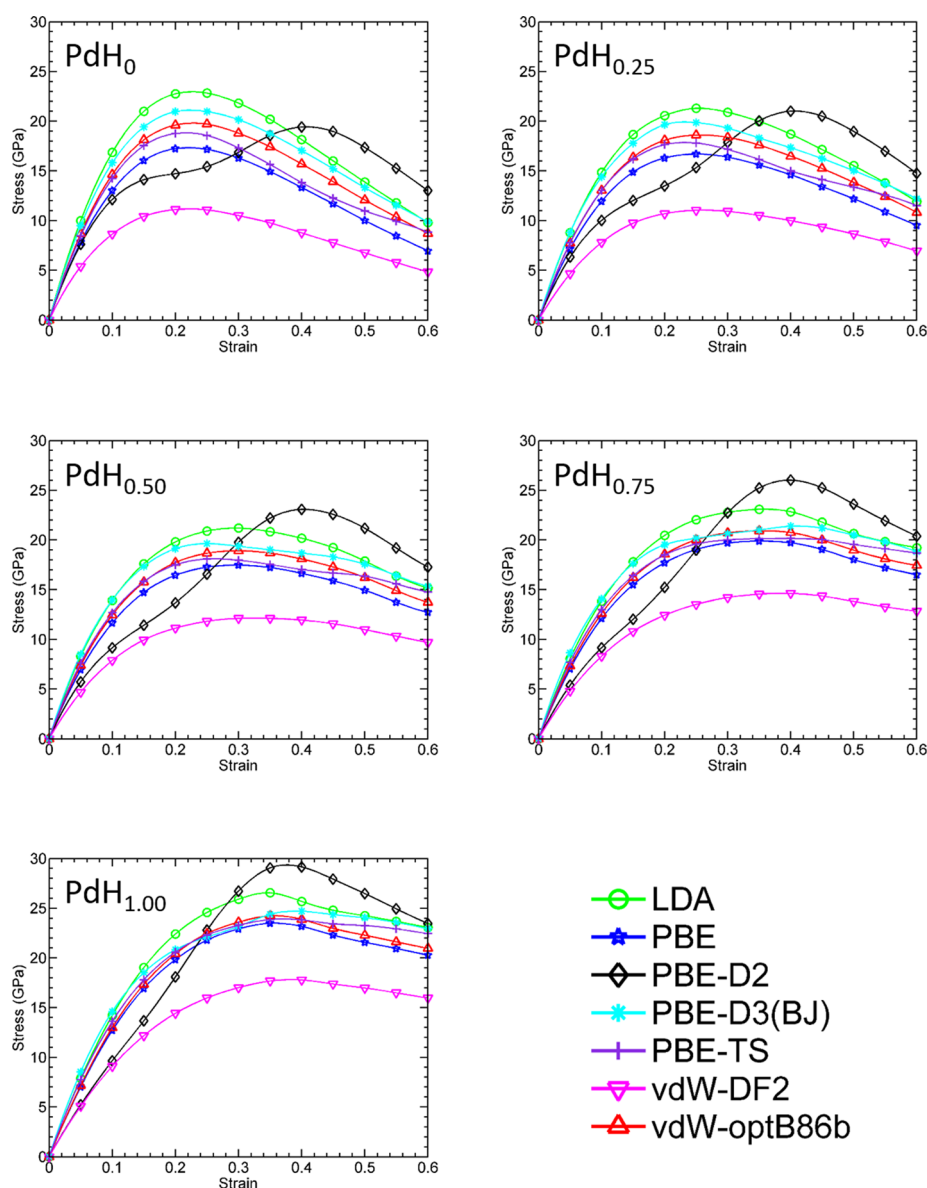


**Figure 5.** Stress–strain curves in  $\text{PdH}_x$  for  $x =$  (a) 0, (b) 0.25, (c) 0.50, (d) 0.75, and (e) 1.00 along the  $[111]$  crystal axis.

tensile stress as a function of strain, we calculated these relaxed energies by varying  $\epsilon$  from 0.00 to 0.60 in increments of 0.01 (i.e., 1% strain). We thus obtained the electronic energy  $E$  as a function of  $\epsilon$  which we then fitted to a piecewise polynomial form of a cubic spline interpolant. The first derivative of this piecewise polynomial was then evaluated numerically to obtain smooth values of the tensile strength as a function of  $\epsilon$ , as required in eq 6.

We carried out all of our tensile strength calculations by applying a uniaxial tensile strain along the 3 individual crystalline directions ( $[100]$ ,  $[110]$ , and  $[111]$ ) for each of the different  $\text{PdH}_x$  stoichiometries in Figure 1. It is worth noting that while the tensile strength calculations along the  $[100]$  direction can be carried out using the primitive unit cells depicted in Figure 1, the tensile strengths for the other  $[110]$  and  $[111]$  directions require the use of larger supercells. It is also worth mentioning that our present study on stress–strain properties for the various  $\text{PdH}_x$  stoichiometries comprises an immense number of DFT calculations, specifically, a total of 6,300 separate DFT relaxations ( $= 60$  strain values  $\times 5$  different

$\text{PdH}_x$  stoichiometries  $\times 7$  different DFT methods  $\times 3$  crystalline directions).

Figures 4 and 5 compare the stress–strain curves among the 7 different DFT methods for the  $[100]$  and  $[111]$  crystalline directions. We omit plots of the  $[110]$  stress–strain curve in the main text since the stress–strain properties along the  $[110]$  direction are known to exhibit qualitatively different characteristics. Specifically, it is well-known in the literature that while bond breaking occurs for  $[100]$  and  $[111]$  strains in face-centered cubic metals, tension in the  $[110]$  direction leads to a phase transformation.<sup>52</sup> As a result, for pure Pd this phase transformation results in a compressive stress in the pulling direction, leading to a counterintuitive result. These complex phase transformations are tangential to our analyses of DFT methods, and we do not discuss the  $[110]$  stress–strain relationships further (plots of the  $[110]$  stress–strain curves, however, are included in the Supporting Information for completeness).

For the LDA, PBE, PBE-D3(BJ), PBE-TS, vdW-DF2, and optB86b-vdW methods only, the plots depicted in Figures 4 and

5 are characteristic of stress–strain curves of most metallic solids.<sup>53</sup> Specifically at small strains, the stress–strain curves exhibit a nearly linear behavior up to a maximum stress; as the strain is increased even further past this point, a more gradual decrease in the stress is observed. This maximum along the stress–strain curve is known as the ideal tensile strength of the material,<sup>53</sup> which is the last state just prior to the onset of instability in the crystal lattice. Mathematically, the ideal tensile strength also corresponds to the inflection point in the total energy–strain curve ( $\partial^2 E/\partial \epsilon^2 = \partial \sigma/\partial \epsilon = 0$ ) and represents the maximum load that the material can sustain without undergoing the instability of necking, which leads inevitably to fracture.

While the stress–strain curves for LDA, PBE, PBE-D3(BJ), PBE-TS, vdW-DF2, and optB86b-vdW appear reasonable, we find that the stress–strain relations predicted by the empirically constructed DFT-D2 method are extremely anomalous. Specifically, for both the [100] and [111] directions (for all 5 PdH<sub>x</sub> stoichiometries), the PBE-D2 functional predicts the ideal strength to occur at  $\epsilon$  values that are nearly *twice as large* compared to the other DFT methods. Interestingly, the anomalous results obtained with PBE-D2 appears to be independent of the hydrogen content in the various systems. Take, for example, all the [100] stress–strain curves shown in Figure 4: the PBE-D2 method predicts the maximum stress to occur at  $\epsilon \sim 0.5$ , whereas *all* the other DFT methods produce a maximum near  $\epsilon \sim 0.3$  instead. The [111] stress–strain curves in Figure 5 show similar anomalous results: the PBE-D2 method yields a maximum stress at  $\epsilon \sim 0.4$  instead of the  $\epsilon \sim 0.25$  value predicted by all the other functionals. To put these anomalous stress values into perspective, recent tensile strength experiments on palladium place the maximum stress at  $\epsilon$  values no larger than 0.2. We also performed simple benchmark tests on other materials (and pseudopotentials) and obtained similar anomalous results from the DFT-D2 method. As such, the results described in this work are expected to apply to a broad range of materials, and we expect the DFT-D2 method to predict strain values that are unphysically too large as well as stress–strain curves that are qualitatively different than any of the other functionals.

It is interesting to mention that for small strain values,  $0.0 < \epsilon < 0.2$  (regimes where DFT-D2 is still valid), we observe the following trends in the computed stress for both Figures 4 and 5: vdW-DF2  $\approx$  PBE-D2  $<$  PBE  $\sim$  PBE-TS  $\sim$  optB86b-vdW  $<$  PBE-D3(BJ)  $<$  LDA. These general trends can be rationalized using the same arguments discussed previously for the cohesive energies. For example, LDA overestimates bond strengths and cohesive energies and, therefore, predicts the largest stress among the DFT methods (within the  $0.0 < \epsilon < 0.2$  range). The optB86b-vdW method lies between the PBE and LDA curves since the nonempirical vdW correlation effects added to the “base” optB86b functional corrects for the lower stress values predicted by the pure PBE GGA. The PBE-D3(BJ) and PBE-TS stress–strain curves yield slightly larger and smaller stresses, respectively, than the optB86b-vdW functional, which also reflects their trends in the cohesive energy. As mentioned previously, the second-generation vdW-DF2 functional significantly underestimates cohesive energies among the tested DFT methods and, therefore, predicts the lowest stress for small strain values. The maximum ideal tensile strengths are presented in Table 3 and summarized in Figure 6. The ideal tensile strengths obtained from PBE-D2 are not tabulated since this functional produces unphysical results, as discussed

**Table 3. Maximum Strength in GPa for PdH<sub>x</sub> Calculated Utilizing Various DFT Methods**

	LDA	PBE	PBE-D3(BJ)	PBE-TS	vdW-DF2	optB86b-vdW
PdH <sub>0</sub>	22.77	17.39	20.82	18.34	11.09	19.52
PdH <sub>0.25</sub>	20.85	15.42	19.10	16.32	9.14	17.53
PdH <sub>0.50</sub>	18.84	13.62	17.36	14.48	7.31	15.65
PdH <sub>0.75</sub>	16.31	11.51	15.02	12.36	5.35	13.25
PdH <sub>1.00</sub>	13.25	8.93	12.37	9.87	3.36	10.70

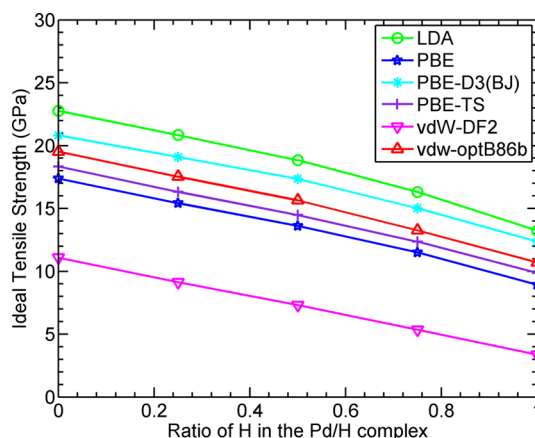


**Figure 6.** Ideal tensile strengths for the PdH<sub>x</sub> system as predicted by the various DFT methods.

previously. However, it is worth noting that for all of the functionals in this study, the maximum ideal strength decreases as the proportion of hydrogen in the palladium system increases. These observations confirm recent experiments that show metal-hydrides are more prone to failure than their pure counterparts<sup>54</sup> and that their maximum tensile strength is inversely proportional to the amount of hydrogen present in the crystal lattice.

Returning to the anomalous stress–strain curves predicted by PBE-D2, it is somewhat surprising that even the simplest functionals (LDA and PBE) yield results that are much more realistic than the “improved” dispersion-corrected DFT-D2 method. We attribute these anomalous results to the (geometry-independent) dispersion coefficients and simple damping functions that are inherent to the empirical DFT-D2 method. To test these claims further, we also carried out DFT-D3(BJ) and DFT-TS single-point energies on top of the previously optimized DFT-D2 geometries. Interestingly, we found that both the DFT-D3(BJ) and DFT-TS single-point energy stress–strain curves (not shown) were nearly identical to their corresponding relaxed-strain curves already shown in Figures 4 and 5. Consequently, the anomalous DFT-D2 stress–strain curves are *not* the result of abnormal DFT-D2 structural optimizations or unusual deformations of the solid; rather, the electronic energies predicted by the empirical DFT-D2 method *itself* give strain energies that are unphysically too large. As the  $C_6$  dispersion energies in DFT-D2 are constructed from simple estimates of *atomic* ionization potentials and static dipole polarizabilities, this simplistic approach is expected to fail in much more complex environments in solids, particularly configurations that are far from equilibrium. It is interesting to note that the *atomic* values for  $C_6$  in DFT-D2, DFT-D3, and DFT-TS are 428, 609, and 158 au, respectively, whereas the *bulk* values for  $C_6$  in DFT-D3 and DFT-TS are correspondingly



266 and 174 au (the atomic and bulk values for  $C_6$  are the same in DFT-D2). Furthermore, to clearly show the variations in  $C_6$  as a function of the applied strain, we plot in Figure 7 the  $C_6$

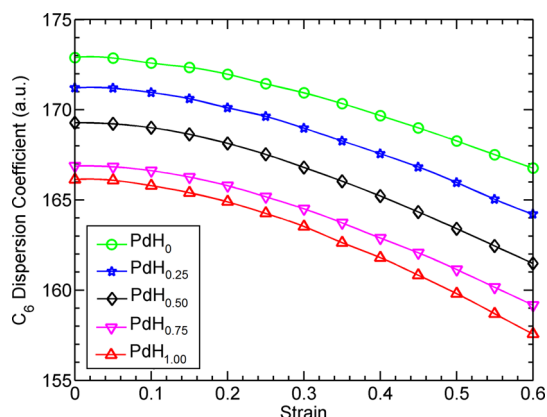


**Figure 7.** Variations in the  $C_6$  dispersion coefficient computed with PBE-TS as a function of the applied strain. The  $C_6$  dispersion coefficient computed with PBE-D2 (not shown) is constant and fixed to 428 au.

values for Pd in all of the various  $\text{PdH}_x$  stoichiometries computed with the PBE-TS functional. Interestingly, Figure 7 clearly shows that the  $C_6$  values can vary quite significantly, ranging from 166 au at equilibrium to 157 au at 60% strain. In contrast, the  $C_6$  value in PBE-D2 is fixed to single value (428 au), and this simple analysis on  $C_6$  indicates the strong dependence of these coefficients on the surrounding chemical environment. Moreover, while it is well-known that DFT-D2 has a tendency to overestimate the binding energies of isolated molecules in the gas phase,<sup>55</sup> we are not aware of any previous studies on highly nonequilibrium properties of bulk solids. In contrast, the PBE-D3(BJ), PBE-TS, and optB86b-vdW functionals take into account van der Waals effects in a less empirical fashion than the pairwise interactions in DFT-D2. All of the former functionals account for screening effects that are particularly important in metals, thereby restoring the qualitatively correct stress–strain trends shown in Figures 4 and 5.

## CONCLUSIONS

In our first benchmarks on palladium-hydride materials, we carried out a series of calculations on static properties, including lattice constants, bulk moduli, and cohesive energies, using representative functionals within the LDA, GGA, DFT-D, and nonlocal vdW DFT families. For these simple static properties, we find that dispersion interactions are *not* negligible and still play a significant role even in these covalently bonded solid structures. Specifically, both the empirically constructed PBE-D2, PBE-D3(BJ), and PBE-TS methods as well as the nonlocal optB86b-vdW dispersion-corrected functional give the best agreement to the experimental lattice constants and cohesive energies. However, the testing of DFT methods on static properties only gives limited information for solid structures near equilibrium, and a more representative analysis requires additional benchmarks on properties far from equilibrium. To further characterize and thoroughly test the various DFT methods at these extreme conditions, we also carried out extensive analyses of nonequilibrium properties including stress–strain relationships and maximum tensile strengths.

Among all the tested functionals, we surprisingly found that the empirically constructed DFT-D2 method gives stress–strain relationships that are extremely anomalous. Specifically, the PBE-D2 functional predicts the ideal strength to occur at  $\epsilon$  values that are nearly *twice as large* compared to the other DFT methods. To the best of our knowledge, this present study is the first to benchmark dispersion-corrected DFT methods on highly nonequilibrium properties of bulk solids and also the first to report the anomalous tensile-strength results produced by DFT-D2 methods.

Our findings have important ramifications for both method development and future parametrizations of structural properties in solids: (1) On a practical note, we find that the next-generation dispersion-corrected methods (i.e., DFT-D3 and DFT-TS) and the nonlocal optB86b-vdW method yield accurate results for *both* equilibrium and nonequilibrium properties. While the DFT-D2 method gives accurate results for lattice constants, bulk moduli, and cohesive energies, the stress–strain curves predicted by DFT-D2 are extremely anomalous and physically incorrect (the opposite is true for the nonlocal vdW-DF2 functional which gives reasonable results for stress–strain properties but poor results for lattice constants, bulk moduli, and cohesive energies). As such, we recommend usage of the PBE-D3(BJ), PBE-TS, or optB86b-vdW functionals for accurately computing both equilibrium and nonequilibrium properties in bulk solids. (2) For future development of new dispersion-corrected DFT functionals, we advocate the inclusion of simple tensile strength benchmarks to ensure that anomalous stress–strain results are not produced. There has already been prior work to include nonequilibrium *molecular* geometries (in vacuum) to construct new dispersion-corrected DFT methods; however, the use of nonequilibrium *solid-state* structures has not been utilized. These nonequilibrium tensile strength tests require relatively small unit cells, and a simple plot of the stress–strain curve can be easily used as a diagnostic for testing the fidelity of new dispersion-corrected functionals. (3) Most importantly, one should proceed with caution in using DFT-D2 (and other coarse-grained parametrizations obtained from DFT-D2) for computing material properties in extreme environments, *particularly for bulk solids*. While the newer dispersion-corrected DFT-D3, DFT-TS, and nonlocal vdW methods are now commonly used for molecular interactions, the older DFT-D2 method is still widely employed for bulk solids, surfaces, and condensed phase systems (a cursory keyword search for “DFT-D2” vs “DFT-D3” in the titles and abstracts of materials science journals in the Thomson Reuters Web of Science<sup>56</sup> yields 41 papers for DFT-D2 and only 12 papers for DFT-D3, during the years 2010–2015). Moreover, there are still ongoing efforts in parametrizing new molecular dynamics force fields and equation-of-state models from DFT-D2 benchmarks.<sup>57–60</sup> While these new force fields and models will give reliable results for properties near equilibrium, one should proceed with caution in using DFT-D2-parametrized methods for properties far from equilibrium (i.e., in extreme stress–strain environments and irreversible phase transformations). For materials under extreme stress/strain conditions, particularly for bulk solids as demonstrated in this work, DFT-D2-based force fields may need to be re-examined or reparametrized.



## ■ ASSOCIATED CONTENT

### ■ Supporting Information

The Supporting Information is available free of charge on the ACS Publications website at DOI: 10.1021/acs.jctc.5b00653.

Plots of stress–strain curves for PdH<sub>x</sub> along the [110] crystal axis (PDF)

## ■ AUTHOR INFORMATION

### Corresponding Author

\*Web: <http://www.bmwong-group.com>. E-mail: [bryan.wong@ucr.edu](mailto:bryan.wong@ucr.edu)

### Notes

The authors declare no competing financial interest.

## ■ ACKNOWLEDGMENTS

We acknowledge the National Science Foundation for the use of supercomputing resources through the Extreme Science and Engineering Discovery Environment (XSEDE), Project No. TG-CHE150040. We also gratefully acknowledge Prof. De-en Jiang for his assistance with the VASP 5.3.5 source code.

## ■ REFERENCES

- (1) Hsieh, H. P. *Inorganic Membranes for Separation and Reaction*; Elsevier Science: 1996; pp 314–315.
- (2) Murray, G.; White, C. V.; Weise, W. *Introduction to Engineering Materials: Behavior, Properties, and Selection*; Taylor & Francis: 1993; Vol. 23–40, pp 448–455.
- (3) Yvon, K.; Schefer, J.; Stucki, F. Structural studies of the hydrogen storage material Mg<sub>2</sub>NiH<sub>4</sub>. 1. Cubic high-temperature structure. *Inorg. Chem.* **1981**, *20*, 2776–2778.
- (4) Klebanoff, L. *Hydrogen Storage Technology: Materials and Applications*; Taylor & Francis: 2012; pp 369–371.
- (5) Agrawal, R.; Espinosa, H. D. Giant Piezoelectric Size Effects in Zinc Oxide and Gallium Nitride Nanowires. A First Principles Investigation. *Nano Lett.* **2011**, *11*, 786–790.
- (6) Hafner, J.; Wolverton, C.; Ceder, G. Toward Computational Materials Design: The Impact of Density Functional Theory on Materials Research. *MRS Bull.* **2006**, *31*, 659–668.
- (7) Lee, B.; Rudd, R. E. First-principles calculation of mechanical properties of Si(001) nanowires and comparison to nanomechanical theory. *Phys. Rev. B* **2007**, *75*, 195328.
- (8) Patil, S. K. R.; Khare, S. V.; Tuttle, B. R.; Bording, J. K.; Kodambaka, S. Mechanical stability of possible structures of PtN investigated using first-principles calculations. *Phys. Rev. B: Condens. Matter Mater. Phys.* **2006**, *73*, 104118.
- (9) Ogata, S.; Umeno, Y.; Kohyama, M. First-principles approaches to intrinsic strength and deformation of materials: perfect crystals, nano-structures, surfaces and interfaces. *Modell. Simul. Mater. Sci. Eng.* **2009**, *17*, 013001.
- (10) Zhao, E.; Wang, J.; Meng, J.; Wu, Z. Structural, mechanical and electronic properties of 4d transition metal mononitrides by first-principles. *Comput. Mater. Sci.* **2010**, *47*, 1064–1071.
- (11) Buehler, M. J. Atomistic and continuum modeling of mechanical properties of collagen: Elasticity, fracture, and self-assembly. *J. Mater. Res.* **2006**, *21*, 1947–1961.
- (12) Laudon, M.; Carlson, N. N.; Masquelier, M. P.; Daw, M. S.; Windl, W. Multiscale modeling of stress-mediated diffusion in silicon: Ab initio to continuum. *Appl. Phys. Lett.* **2001**, *78*, 201–203.
- (13) Lidorikis, E.; Bachlechner, M. E.; Kalia, R. K.; Nakano, A.; Vashishta, P.; Voyiadis, G. Z. Coupling Length Scales for Multiscale Atomistics-Continuum Simulations: Atomistically Induced Stress Distributions in Si/Si<sub>3</sub>N<sub>4</sub> Nanopixels. *Phys. Rev. Lett.* **2001**, *87*, 086104.
- (14) Lyubartsev, A.; Tu, Y.; Laaksonen, A. Hierarchical Multiscale Modelling Scheme from First Principles to Mesoscale. *J. Comput. Theor. Nanosci.* **2009**, *6*, 951–959.
- (15) Lu, Q.; Gao, W.; Huang, R. Atomistic simulation and continuum modeling of graphene nanoribbons under uniaxial tension. *Modell. Simul. Mater. Sci. Eng.* **2011**, *19*, 054006.
- (16) Ramasubramaniam, A.; Carter, E. A. Coupled Quantum–Atomistic and Quantum–Continuum Mechanics Methods in Materials Research. *MRS Bull.* **2007**, *32*, 913–918.
- (17) Spanos, G.; Geltmacher, A. B.; Lewis, A. C.; Bingert, J. F.; Mehl, M.; Papaconstantopoulos, D.; Mishin, Y.; Gupta, A.; Matic, P. A methodology to aid in the design of naval steels: Linking first principles calculations to mesoscale modeling. *Mater. Sci. Eng., A* **2007**, *452–453*, 558–568.
- (18) Wernik, J.; Meguid, S. Atomistic-based continuum modeling of the nonlinear behavior of carbon nanotubes. *Acta Mech* **2010**, *212*, 167–179.
- (19) Yasi, J. A.; Hector, L. G., Jr; Trinkle, D. R. First-principles data for solid-solution strengthening of magnesium: From geometry and chemistry to properties. *Acta Mater.* **2010**, *58*, 5704–5713.
- (20) Hale, L. M.; Wong, B. M.; Zimmerman, J. A.; Zhou, X. W. Atomistic potentials for palladium-silver hydrides. *Modell. Simul. Mater. Sci. Eng.* **2013**, *21*, 045005.
- (21) Zhou, X. W.; Zimmerman, J. A.; Wong, B. M.; Hoyt, J. J. An embedded-atom method interatomic potential for Pd-H alloys. *J. Mater. Res.* **2008**, *23*, 704–718.
- (22) Tsuji, J. *Palladium Reagents and Catalysts: New Perspectives for the 21st Century*; John Wiley & Sons, Inc.: 2004; pp 1–26.
- (23) Drahl, C. Palladium's Hidden Talent. *Chem. Eng. News* **2008**, *86*, 53–56.
- (24) Shu, J.; Grandjean, B. P. A.; Neste, A. V.; Kaliaguine, S. Catalytic palladium-based membrane reactors: A review. *Can. J. Chem. Eng.* **1991**, *69*, 1036–1060.
- (25) Antolini, E. Palladium in fuel cell catalysis. *Energy Environ. Sci.* **2009**, *2*, 915–931.
- (26) Manchester, F. D.; San-Martin, A.; Pitre, J. M. The H-Pd (hydrogen-palladium) System. *J. Phase Equilib.* **1994**, *15*, 62–83.
- (27) Grochala, W.; Edwards, P. P. Thermal decomposition of the non-interstitial hydrides for the storage and production of hydrogen. *Chem. Rev.* **2004**, *104*, 1283–1315.
- (28) Barnoush, A.; Vehoff, H. Recent developments in the study of hydrogen embrittlement: Hydrogen effect on dislocation nucleation. *Acta Mater.* **2010**, *58*, 5274–5285.
- (29) Huang, C. S.; Kim, M.; Wong, B. M.; Safron, N. S.; Arnold, M. S.; Gopalan, P. Raman Enhancement of a Dipolar Molecule on Graphene. *J. Phys. Chem. C* **2014**, *118*, 2077–2084.
- (30) Johnson, P. S.; Huang, C. S.; Kim, M.; Safron, N. S.; Arnold, M. S.; Wong, B. M.; Gopalan, P.; Himpsel, F. J. Orientation of a Mono layer of Dipolar Molecules on Graphene from X-ray Absorption Spectroscopy. *Langmuir* **2014**, *30*, 2559–2565.
- (31) Wong, B. M.; Ye, S. H. Self-assembled cyclic oligothiophene nanotubes: Electronic properties from a dispersion-corrected hybrid functional. *Phys. Rev. B: Condens. Matter Mater. Phys.* **2011**, *84*, 075115.
- (32) Wong, B. M.; Ye, S. H.; O'bryan, G. Reversible, optomechanically induced spin-switching in a nanoribbon-spiropyran hybrid material. *Nanoscale* **2012**, *4*, 1321–1327.
- (33) Klimeš, J.; Bowler, D. R.; Michaelides, A. Van der Waals density functionals applied to solids. *Phys. Rev. B: Condens. Matter Mater. Phys.* **2011**, *83*, 195131.
- (34) Gráfová, L.; Pitoňák, M.; Řezáč, J.; Hobza, P. Comparative Study of Selected Wave Function and Density Functional Methods for Noncovalent Interaction Energy Calculations Using the Extended S22 Data Set. *J. Chem. Theory Comput.* **2010**, *6*, 2365–2376.
- (35) Marom, N.; Tkatchenko, A.; Rossi, M.; Gobre, V. V.; Hod, O.; Scheffler, M.; Kronik, L. Dispersion Interactions with Density-Functional Theory: Benchmarking Semiempirical and Interatomic Pairwise Corrected Density Functionals. *J. Chem. Theory Comput.* **2011**, *7*, 3944–3951.
- (36) Grimme, S. Semiempirical GGA-type density functional constructed with a long-range dispersion correction. *J. Comput. Chem.* **2006**, *27*, 1787–1799.

- (37) Grimme, S.; Antony, J.; Ehrlich, S.; Krieg, H. A consistent and accurate ab initio parametrization of density functional dispersion correction (DFT-D) for the 94 elements H-Pu. *J. Chem. Phys.* **2010**, *132*, 154104.
- (38) Tkatchenko, A.; Scheffler, M. Accurate Molecular Van Der Waals Interactions from Ground-State Electron Density and Free-Atom Reference Data. *Phys. Rev. Lett.* **2009**, *102*, 073005.
- (39) Ruiz, V. G.; Liu, W.; Zojer, E.; Scheffler, M.; Tkatchenko, A. Density-Functional Theory with Screened van der Waals Interactions for the Modeling of Hybrid Inorganic-Organic Systems. *Phys. Rev. Lett.* **2012**, *108*, 146103.
- (40) Roman-Perez, G.; Soler, J. M. Efficient Implementation of a van der Waals Density Functional: Application to Double-Wall Carbon Nanotubes. *Phys. Rev. Lett.* **2009**, *103*, 096102.
- (41) Dion, M.; Rydberg, H.; Schroder, E.; Langreth, D. C.; Lundqvist, B. I. Van der Waals density functional for general geometries. *Phys. Rev. Lett.* **2004**, *92*, 246401.
- (42) Grimme, S.; Ehrlich, S.; Goerigk, L. Effect of the damping function in dispersion corrected density functional theory. *J. Comput. Chem.* **2011**, *32*, 1456–1465.
- (43) Becke, A. D.; Johnson, E. R. A density-functional model of the dispersion interaction. *J. Chem. Phys.* **2005**, *123*, 154101.
- (44) Johnson, E. R.; Becke, A. D. A post-Hartree–Fock model of intermolecular interactions. *J. Chem. Phys.* **2005**, *123*, 024101.
- (45) Johnson, E. R.; Becke, A. D. A post-Hartree-Fock model of intermolecular interactions: Inclusion of higher-order corrections. *J. Chem. Phys.* **2006**, *124*, 174104.
- (46) Kronik, L.; Tkatchenko, A. Understanding Molecular Crystals with Dispersion-Inclusive Density Functional Theory: Pairwise Corrections and Beyond. *Acc. Chem. Res.* **2014**, *47*, 3208–3216.
- (47) Lee, K.; Murray, E. D.; Kong, L. Z.; Lundqvist, B. I.; Langreth, D. C. Higher-accuracy van der Waals density functional. *Phys. Rev. B: Condens. Matter Mater. Phys.* **2010**, *82*, 081101(R).
- (48) Csonka, G. I.; Perdew, J. P.; Ruzsinszky, A.; Philipson, P. H. T.; Lebègue, S.; Paier, J.; Vydrov, O. A.; Ángyán, J. G. Assessing the performance of recent density functionals for bulk solids. *Phys. Rev. B: Condens. Matter Mater. Phys.* **2009**, *79*, 155107.
- (49) Chakarova-Käck, S. D.; Schröder, E.; Lundqvist, B. I.; Langreth, D. C. Application of van der Waals Density Functional to an Extended System: Adsorption of Benzene and Naphthalene on Graphite. *Phys. Rev. Lett.* **2006**, *96*, 146107.
- (50) Puzder, A.; Dion, M.; Langreth, D. C. Binding energies in benzene dimers: Nonlocal density functional calculations. *J. Chem. Phys.* **2006**, *124*, 164105.
- (51) Murray, E. D.; Lee, K.; Langreth, D. C. Investigation of Exchange Energy Density Functional Accuracy for Interacting Molecules. *J. Chem. Theory Comput.* **2009**, *5*, 2754–2762.
- (52) Morris, J. W.; Clatterbuck, D. M.; Chrzan, D. C.; Krenn, C. R.; Luo, W.; Cohen, M. L. Elastic stability and the limits of strength. *Mater. Sci. Forum* **2003**, 426–432, 4429–4434.
- (53) Beer, F. P.; Johnston, E. R., Jr.; DeWolf, J. T.; Mazurek, D. F. *Mechanics of Materials*, 7th ed.; McGraw-Hill Science/Engineering/Math: 2011; pp 47–121.
- (54) Dillon, E.; Jimenez, G.; Davie, A.; Bulak, J.; Nesbit, S.; Craft, A. Factors influencing the tensile strength, hardness, and ductility of hydrogen-cycled palladium. *Mater. Sci. Eng., A* **2009**, *524*, 89–97.
- (55) Brndiar, J.; Stich, I. van der Waals Interaction Energies of Small Fragments of P, As, Sb, S, Se, and Te: Comparison of Complete Basis Set Limit CCSD(T) and DFT with Approximate Dispersion. *J. Chem. Theory Comput.* **2012**, *8*, 2301–2309.
- (56) Web of Science. <http://apps.webofknowledge.com/> (accessed September 4, 2015).
- (57) Fang, H.; Kamakoti, P.; Zang, J.; Cundy, S.; Paur, C.; Ravikovitch, P. I.; Sholl, D. S. Prediction of CO<sub>2</sub> Adsorption Properties in Zeolites Using Force Fields Derived from Periodic Dispersion-Corrected DFT Calculations. *J. Phys. Chem. C* **2012**, *116*, 10692–10701.
- (58) Tuttle, T.; Thiel, W. OMx-D: semiempirical methods with orthogonalization and dispersion corrections. Implementation and biochemical application. *Phys. Chem. Chem. Phys.* **2008**, *10*, 2159–2166.
- (59) Zang, J.; Nair, S.; Sholl, D. S. Prediction of Water Adsorption in Copper-Based Metal–Organic Frameworks Using Force Fields Derived from Dispersion-Corrected DFT Calculations. *J. Phys. Chem. C* **2013**, *117*, 7519–7525.
- (60) Jensen, B. D.; Wise, K. E.; Odegard, G. M. Simulation of the Elastic and Ultimate Tensile Properties of Diamond, Graphene, Carbon Nanotubes, and Amorphous Carbon Using a Revised ReaxFF Parametrization. *J. Phys. Chem. A* **2015**, *119*, 9710–9721.